

A MEMS rotary comb mechanism for harvesting the kinetic energy of planar vibrations

This article has been downloaded from IOPscience. Please scroll down to see the full text article.

2010 J. Micromech. Microeng. 20 065017

(<http://iopscience.iop.org/0960-1317/20/6/065017>)

View [the table of contents for this issue](#), or go to the [journal homepage](#) for more

Download details:

IP Address: 218.186.8.11

The article was downloaded on 14/05/2010 at 14:32

Please note that [terms and conditions apply](#).

A MEMS rotary comb mechanism for harvesting the kinetic energy of planar vibrations

Bin Yang^{1,4}, Chengkuo Lee^{1,2,4,5}, Rama Krishna Kotlanka², Jin Xie²
and Siak Piang Lim³

¹ Department of Electrical & Computer Eng., National University of Singapore,
4 Eng. Drive 3, Singapore 117576

² Institute of Microelectronics (IME), A*STAR (Agency for Science, Technology and Research),
11 Science Park Road, Singapore Science Park II, Singapore 117685

³ Department of Mechanical Eng., National University of Singapore, 9 Eng. Drive 1, Singapore 117576

E-mail: elelc@nus.edu.sg

Received 25 February 2010, in final form 15 April 2010

Published 14 May 2010

Online at stacks.iop.org/JMM/20/065017

Abstract

A capacitive energy harvester based on in-plane rotary combs is proposed and studied. It is capable of collecting kinetic energy from planar ambient vibrations for low frequency operation. The design and simulation of capacitance among rotary combs, ladder spring and resonant frequency of the whole rotary comb energy harvester are presented in this paper. This device is fabricated in SOI (silicon-on-insulator) wafers by deep silicon etching technology. The dimensions of the prototype are about 7.5 mm × 7.5 mm × 0.7 mm. A maximum measured output power in air for vibrations of 0.5 g, 1 g, 1.5 g, 2 g and 2.5 g is 0.11 μW, 0.17 μW, 0.24 μW, 0.3 μW and 0.35 μW, respectively, when the loading resistance matches the parasitic resistance of 80 MΩ at the resonant frequency of 110 Hz. In order to reduce the air damping effect, the prototype is packaged by having a metal cap to form the vacuum level of 3 Torr. The testing results in vacuum level of 3 Torr show that the resonant frequency decreases from 110 Hz in air to 63 Hz, and the maximum electrical output power at 0.25 g is 0.39 μW.

(Some figures in this article are in colour only in the electronic version)

1. Introduction

Microelectromechanical systems (MEMS)-based energy harvesters are developed to recharge the battery and extend its lifetime to be used in implantable biomedical devices, wireless sensor nodes and devices operated in harsh environment [1–5]. Harvesting body heat and converting heat energy into electrical energy is one of the promising approaches [6–10], and the other approaches of energy harvesting are mainly collecting and converting energy from vibrations, i.e. clean and continuous (but with varying intensities) energy sources. There are three kinds of energy transduction mechanisms to generate electricity from vibration, namely electrostatic [11–15], electromagnetic [2, 16–20] and piezoelectric

mechanisms [1, 21–25]. Hoffmann *et al* have reported that at micro-scale, an electrostatic MEMS energy harvester is the favored approach. The energy transduction coefficient of electromagnetic mechanism decreases ten times faster than the one of the electrostatic mechanism when the volume of the MEMS energy harvester shrinks to 1% of original size [26]. Upon the traditional categorization, there are three different types of electrostatic energy harvesters depending on how the capacitor electrode plates are configured, i.e. in-plane overlap varying type, in-plane gap closing type and out-of-plane gap closing type. During operation, the capacitor electrodes are required to be biased via an external voltage source, and the movable electrode of the capacitor electrodes will engage and disengage due to external vibrations such that the created capacitor is varied as a function of ambient vibrations [11–14, 28, 29]. Recently Basset *et al* have presented a novel

⁴ Both authors contributed equally as the first author.

⁵ Author to whom any correspondence should be addressed.

silicon-based and batch-processed MEMS electrostatic harvester [30, 31]. The output power of 61 nW on a 60 M Ω resistive load under a vibration level of 0.25 g at 250 Hz is reported. To get rid of the requirement of external bias, an electret layer is introduced to form an electrical potential and then electricity is harvested from alternately changed relative positions of electrodes due to vibrations. Various electrostatic energy harvesters using an electret layer have been reported so far [32–39]. For example, Boland *et al* [32] have reported a rotational electret power generator with a rotor of 8 mm diameter and demonstrated the output power of 25 μ W, while Tsutsumino *et al* [35] have developed a seismic electret generator with 20 \times 20 mm² grid electrets/electrodes and with an output power of 0.28 mW.

On the other hand, the reported electrostatic energy harvesters comprise a set of springs which are softer regarding the moving direction of a mass along the first axis, i.e. linear motion, and are stiffer in the two axes perpendicular to the first moving axis. As a result, most electrostatic mechanisms are designed to harvest kinetic energy of linear motion. However, the vibrations from the natural resources may not always be along one direction. A pendulum-like vibration swing trace, i.e. planar motion, is often seen. It is to be noted that planar vibrations comprising two components of kinetic energy along two axes are common in the natural environment. Besides, various ambient vibration sources have been reported [4], for instance, a small microwave oven with the peak acceleration of 2.5 m s⁻² at the resonant frequency of 121 Hz, a washing machine with the peak acceleration of 0.5 m s⁻² at 109 Hz, a kitchen blender casing with the acceleration of 6.4 m s⁻² at 121 Hz and a CD on notebook computer with the peak acceleration of 0.6 m s⁻² at 75 Hz [4]. The concept of a resonant rotating mass fixed on a spiral spring has been proposed as an inertial mechanism for harvesting kinetic energy from rotational motion, i.e. a kind of planar motion [15, 40]. Recently, Bartsch *et al* have reported a two-dimensional electret-based resonant micro energy harvester to extract energy from ambient vibrations with arbitrary planar motion directions. It shows resonant frequencies and extracted harvester powers depending on the design of the circular spring system and capacitor dimensions within the 0.3–2 kHz and 1–100 pW ranges [41].

Electret-based electrostatic energy harvesters do not require external biases, but the specific electret layer is needed. In view of the fact that integration of the MEMS energy harvester and microelectronics on the same chip is an essential approach for the realization of self-powered microelectronics, development of CMOS compatible processes for making silicon MEMS energy harvesters is preferred. In this paper, in order to overcome the complicated fabrication process, an electrostatic MEMS energy harvester without using an electret layer is fabricated from an 8'' silicon-on-insulator (SOI) wafer with only two masks. This new energy harvester comprises novel rotary comb electrodes. Upon planar vibrations, the variable capacitor of the rotary comb under bias is characterized with respect to ambient vibrations of various accelerations. The preliminary results show that this new device provides an intriguing alternative for harvesting energy from planar vibrations.

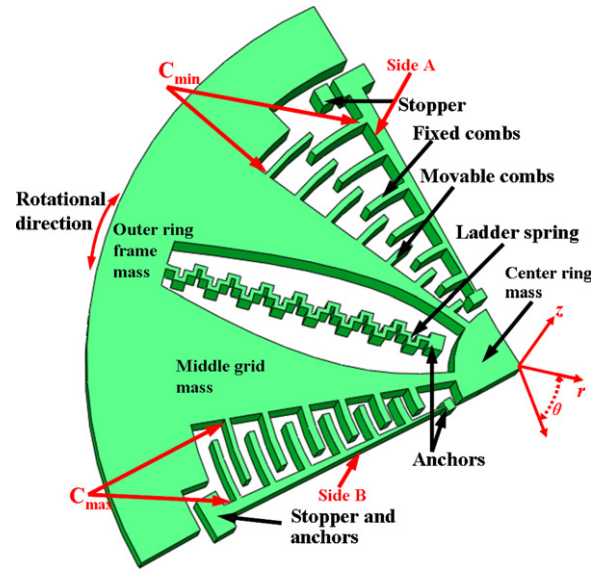


Figure 1. One-sixth schematic drawing of the electrostatic harvester because of the structural symmetry, which includes two sets of movable and fixed combs, ladder spring, stopper and proof mass.

2. Mechanical design and simulation

2.1. Principle of operation

Rotary comb actuators (i.e. using rotational in-plane overlap varying type of electrodes) with a pivot or a virtual anchor at the center of circle formed by the rotary comb have been investigated as actuators for driving a vertical micromirror to move along a trace formed by radial line scanning against the pivot [42, 43]. The rotary comb structure is typically formed by etching and releasing the vertical comb finger structure from the silicon device layer of a silicon-on-insulator (SOI) substrate. With the help of integrated micromirrors, rotary comb actuators have successfully been applied to tunable external cavity diode lasers, variable optical attenuators and optical switches [44–47].

A MEMS energy harvester using rotary comb electrodes will convert the kinetic energy of planar vibration from ambient sources and store it as electrical energy. A schematic drawing of the one-sixth portion of the rotary comb-based electrostatic energy harvester is shown in figure 1. The suspended silicon structure consists of 12 sets of fixed combs, grid-like proof mass integrated with movable combs, six ladder springs and stoppers for avoiding a pull-in phenomenon between movable and fixed combs. In this design, the proof mass is composed of a center ring mass, outer ring frame mass and middle grid mass between them. The outer end of the spring connects with the outer ring frame mass, while the inner end is fixed at the anchor. When an external acceleration is exerted on the rotary comb energy harvester, the movable mass with a rotary comb rotates such that one side of the movable combs engages further inside a set of fixed combs on the same side, i.e. side A, and the opposite side of the movable combs moves away from another set of fixed combs at the opposite side, i.e. side B. There is a 180° phase shift

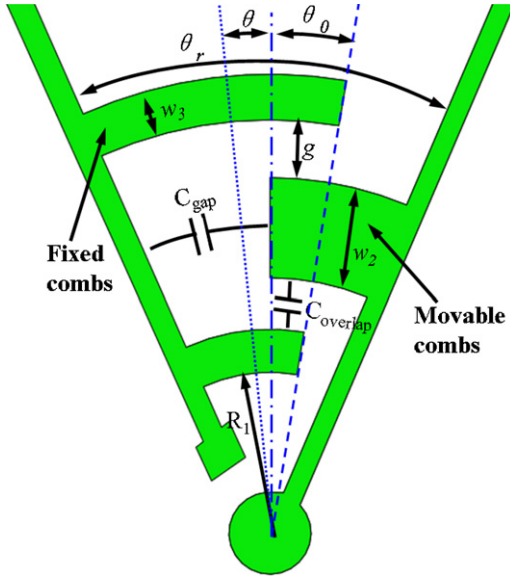


Figure 2. The lumped models for one set of fixed and movable combs. The total capacitance C_{total} consists of the overlap capacitance $C_{overlap}$ and gap capacitance C_{gap} .

between the minimum capacitance of six sets, i.e. defined as C_{min} , and the maximum capacitance of the other six sets, i.e. defined as C_{max} . The rotary comb energy harvester is designed to work on resonant mode. During one rotational vibration cycle, the rotary comb electrodes on side A reach C_{max} at the boundary of rotation swing trace, and reach C_{min} at the other boundary of rotation swing trace.

2.2. Rotary comb capacitance

Figure 2 shows the lumped model for one set of movable and fixed combs. When the movable combs are applied with the excited acceleration, the initial overlap θ_0 is rotated by an angle θ , which results in the total overlap angle $\theta_0 + \theta$ between the concentric interdigitated combs. The total capacitance C_{total} consists of the overlap capacitance $C_{overlap}$ and gap capacitance C_{gap} . All of these gaps are assumed to be parallel plates to simplify the derivation model [46]. Hence, the total capacitance can be calculated by Gauss's law:

$$C_{total} = C_{overlap} + C_{gap}. \quad (1)$$

The overlap capacitance for comb fingers is given by

$$C_{overlap} = \epsilon t (\theta + \theta_0) \times A(n) \quad (2)$$

where

$$A(n) = \sum_{i=1}^n \left\{ \left[\ln \left(\frac{R_1 + 2(i-1)(W_f + g)}{R_1 + 2(i-1)(W_f + g) - g} \right) \right]^{-1} + \left[\ln \left(\frac{R_1 + (2i-1)(W_f + g)}{R_1 + (2i-1)(W_f + g) - g} \right) \right]^{-1} \right\} - \left[\ln \left(\frac{R_1}{R_1 - g} \right) \right]^{-1}$$

$$W_f = (w_2 + w_3)/2.$$

The gap capacitance can be calculated by

$$C_{gap} = \epsilon t W_f B(n) \frac{1}{\frac{\theta_r - \theta_0}{2} - \theta} \quad (3)$$

where

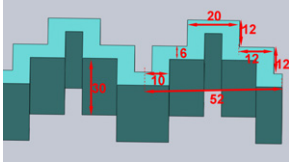
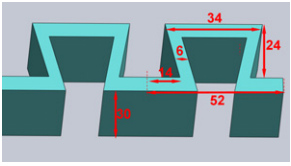
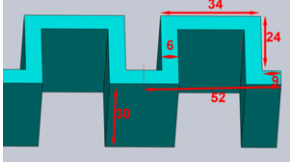
$$B(n) = \sum_{i=1}^n \left\{ \frac{1}{R_1 + 2(i-1)(W_f + g)} + \frac{1}{R_1 + (2i-1)(W_f + g)} \right\}$$

where ϵ is the free-space permittivity with a value of 8.854×10^{-6} pF μm^{-1} , t is the thickness of combs, R_1 is the radius of the concave surface of the first movable combs, g is the gap between fixed and movable combs, w_2 is the width of movable combs, w_3 is the width of fixed combs and θ_r is the initial angle between fixed and movable arms.

2.3. Mechanical spring design

The shape of the spring determines the effective stiffness. For the requirement of substantial rotation of an energy harvester at low excited acceleration loading, the mechanical springs behave compliantly in the angular direction (i.e. rotation) as well as function stiffly in the radial direction (i.e. orthogonal to rotation). The other requirement is to enable the proof mass to rotate in-plane but not to wobble out-of-plane. It means that the ratio of the radial spring constant (K_r) to the rotational spring constant (K_θ), and the ratio of the spring constant along the vertical axis (K_z) to the rotational spring constant (K_θ) should be maintained as large as possible. Its points out that a smaller rotational spring constant (K_θ) is preferred. Three types of mechanical springs including ladder, mountain and serpentine springs with the detailed dimensions are investigated and listed in table 1. The finite element analysis (FEA) is deployed to simulate and calculate the spring constants in different directions. The thickness and total length of the spring are 30 μm and 1960 μm , respectively. An eight-node brick element is used to mesh the models. For larger deformation, nonlinear behavior must be taken into account in ANSYS. The mechanical springs gradually stiffen as the deformation enlarges. In this design, the range of rotational deformation is several micrometers. All the degrees of freedom at one end of the spring are set to be zero, i.e. an anchor of the spring, while the other free end of the spring is assigned with radial and rotational loading conditions to calculate the spring constant in the direction of r , z , θ , respectively, as shown in figure 1. The ratios of spring constants along different directions of the ladder, mountain and serpentine springs are summarized in table 1. The ladder spring has the highest ratios of K_r/K_θ and K_z/K_θ . It means that the ladder spring exhibits better capability in larger rotational angle under the same excited vibration acceleration, while the vertical displacement and translational displacement are suppressed. It implies that the ladder spring performs more linearly. Meanwhile, the three types of springs have similar values of the stiffness ratio

Table 1. Comparison of stiffness for different types of spring designs.

Type	Ladder	Mountain	Serpentine
Dimension (μm)			
K_r/K_θ	78.7	75.74	65.3
K_z/K_r	21.17	21.38	23.23
K_z/K_θ	1666.6	1619.7	1517.98

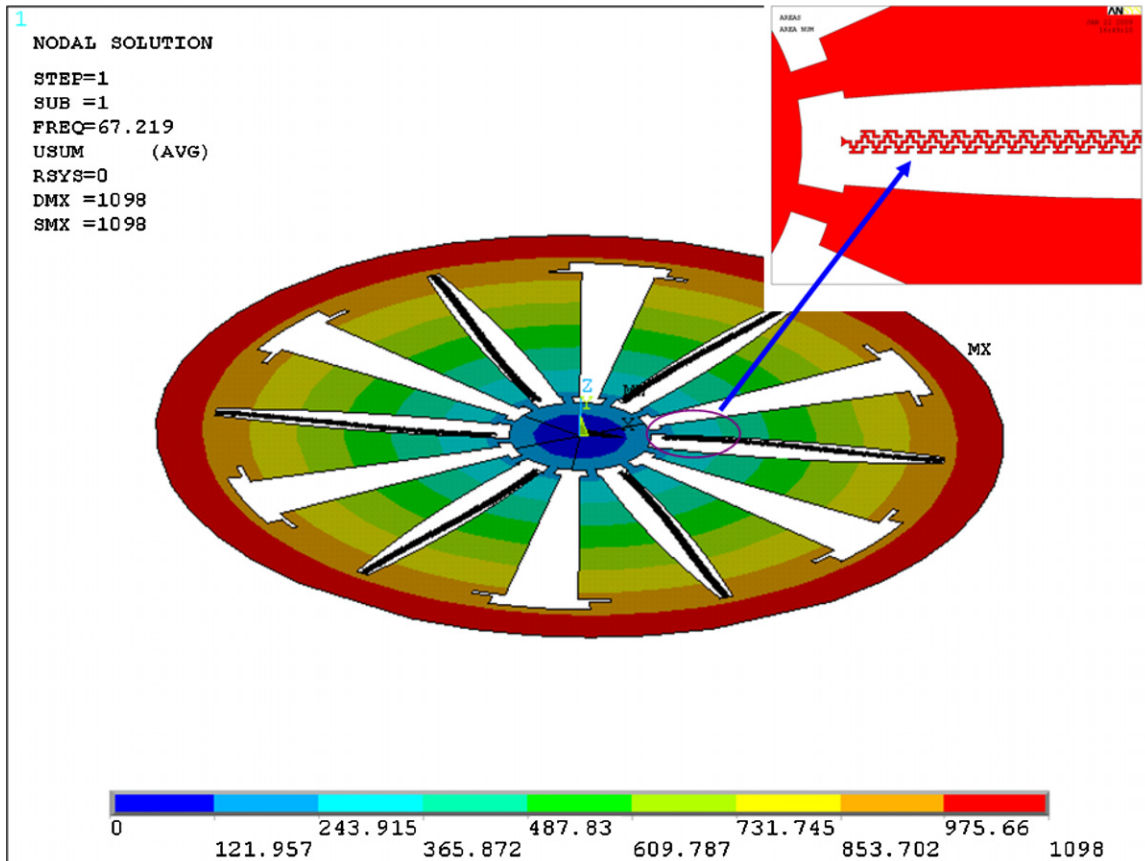


Figure 3. Finite element simulations for the first resonant vibration mode. It shows that the first resonant frequency is 67.2 Hz and its vibration mode is rotational mode.

(i.e. K_z/K_r) in the nonlinear deformation region, implying comparable stability performance. The values in table 1 only apply for the dimensions we have assumed for these three springs. The analysis is not meant to state the superiority of ladder, mountain and serpentine spring types over each other. We are only emphasizing that the ladder spring is suited (under the set of dimensions considered) for the current energy harvester application.

2.4. Resonant frequency simulation

The occurrence of radial instability implies that the equilibrium of electromechanical energy in the radial direction is no longer maintained; that is, the energy released by the comb-drives

exceeds the energy absorption capability of the mechanical springs [27]. In order to maintain radial stability, six ladder springs are distributed symmetrically along the circumferential direction. All anchors are located at the center part. The corresponding frequency of the large peak in magnitude for many commonly occurring vibration sources is below 150 Hz [4], which can be referred to as main design consideration. Based on the calculation equation of resonant frequency, there are two methods to obtain low resonant frequency, i.e. increasing the proof mass and reducing the spring constant. There are three types of masses in our structural design, including the center ring mass, the outer ring frame mass and the middle grid mass between them. Because the thickness of the device layer (30 μm device layer of the SOI wafer)

is very thin compared to the radial dimension of the whole structure (its diameter is about 6 mm), the whole device structure is modeled using three-dimensional (3D) elastic shell elements (SHELL63 element) in the commercial software package ANSYS. Due to computing capacity limitation, it is necessary to simplify of the elaborate features in the actual structure in the FEA model. In this model, the gap between combs and small release holes in a mass is neglected. The Block–Lanczos method modal analysis is employed to predict the vibration mode and its corresponding resonant frequency.

Figure 3 shows the FEA simulation results of vibration for the rotary comb energy harvester. The results show that the first vibration mode is in-plane rotational mode around the z axis and its resonant frequency is 67.2 Hz which meets our design requirements. The resonant frequency of the second mode (out-of-plane rotational mode around the x axis) and the third mode (out-of-plane rotational mode along the y axis) are 145.3 and 145.5 Hz, respectively. These two modes are far away from the first mode, i.e. the device operation mode, such that interference between operation and the other modes is avoided. Moreover, the out-of-plane rotational mode will not be excited during the vibration due to the mismatch between their mode shapes and the excitation motion from the shaker.

3. Fabrication process of the MEMS energy harvester

The rotary comb energy harvester is fabricated by silicon-on-insulator (SOI)-based micromachining technology as shown in figure 4. The SOI wafer used has a 30 μm thick heavily doped device layer, 2 μm thick buried oxide (BOX) layer and a 680 ± 10 μm thick silicon substrate. A 0.75 μm aluminum metal layer is sputtered on the SOI wafer and patterned to

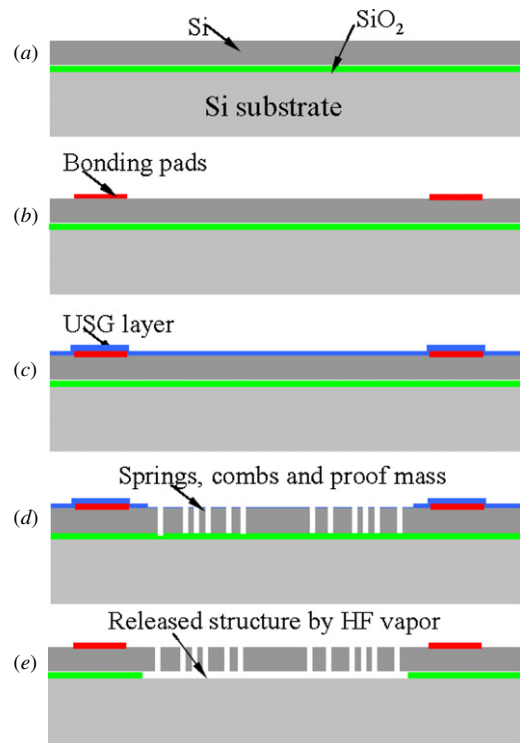


Figure 4. Fabrication process flow: (a) 30 μm SOI wafer; (b) deposition of a 0.75 μm aluminum metal layer; (c) PECVD 5000 Å undoped silicon glass, pattern and RIE; (d) DRIE of 30 μm springs, combs and proof mass; (e) HF vapor to release in order to avoid stiction.

form wire bonding pads. A 5000 Å PECVD undoped silicon glass (USG) is deposited as an insulating layer. After a photolithography pattern transfer process, the hard mask layer of 5000 Å USG is prepared on the silicon device layer by

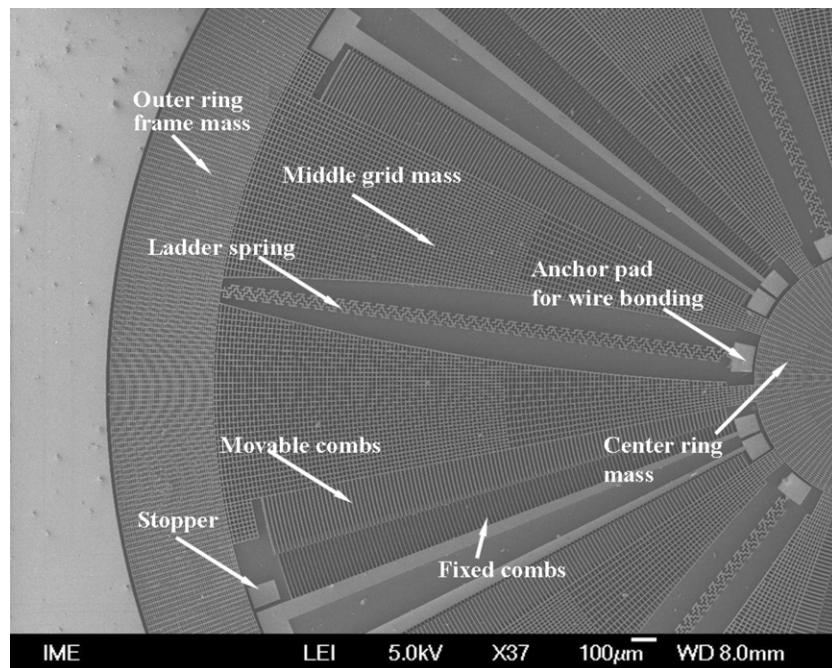


Figure 5. SEM microphoto of a part of the fabricated device.

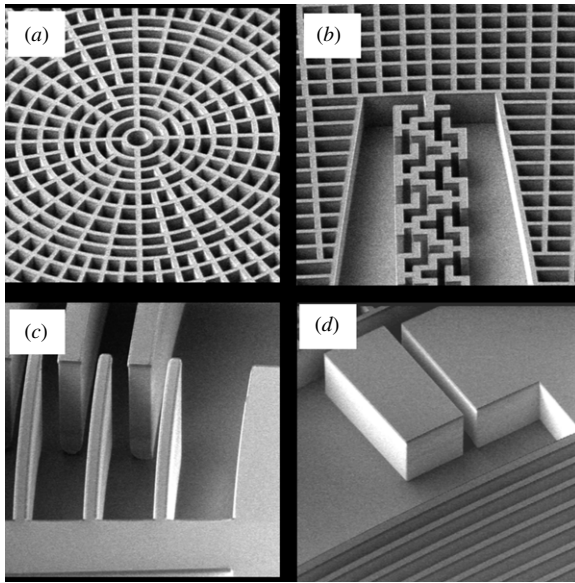


Figure 6. Located enlarged SEM: (a) center ring mass; (b) outer ring frame mass with a ladder spring (the features extending from the peaks of the ladder spring serve as compensation elements for the DRIE process); (c) fixed and movable combs and (d) anchors and stopper.

Table 2. The structural dimensions of the prototype.

Parameter	Description	Value
L	Length of the device structure	7.5 mm
W	Width of the device structure	7.5 mm
T	Thickness of the device structure	0.7 mm
D	Diameter of the movable mass	6 mm
t	Thickness of the movable mass	30 μm
n	Number of springs	6
w_1	Width of the spring comb	6 μm
l_1	Length of the spring	1.96 mm
w_2	Width of the movable comb	5.6 μm
w_3	Width of the fixed comb	3 μm
g	Gap between the fixed and movable combs	3.6 μm

reactive ion etching (RIE). As shown in step (c) of figure 4, the rotary comb energy harvester is made from the 30 μm silicon device layer of the SOI wafer by the deep-reactive ion etching (DRIE) technology. In this step, the mixture gas of C_4F_8 , SF_6 and O_2 is provided in an inductively coupled plasma (ICP) system, where C_4F_8 is used as the passivation precursor, and SF_6 and O_2 serve as the etching gases. In order to avoid cracking in the process of dicing after the release of whole structure, the dicing process for small chips is first employed before the release process. HF vapor is used to etch away a silicon oxide layer in order to release the energy harvester structure from the substrate. Figure 5 shows the top view of the fabricated devices. Figures 6(a)–(d) show close-up views of the center ring mass, outer ring frame mass with the connected ladder spring, combs and stoppers, respectively. Table 2 shows the dimensions of the fabricated prototype in detail.

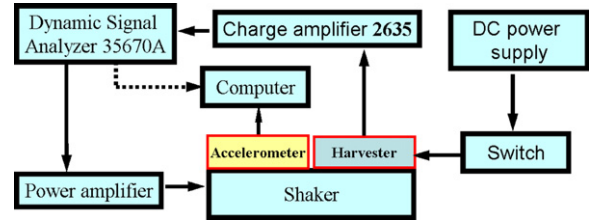


Figure 7. Testing platform.

4. Measurement and discussion

Figure 7 shows the testing platform. This setup consists of a dynamic signal analyzer (Agilent 35670A), a power amplifier (Brüel & Kjær WQ1108, Demark), an electromagnetic shaker (Gearing & Watson Electronics Ltd V20, UK), accelerometer (ADI iSensor GS09001, USA), charge amplifier (Brüel & Kjær model type 2635, Demark) and dc power supply (Agilent model E3631A). The accelerometer connected with a computer through the GPIB port is attached to the shaker in order to measure the input acceleration. The dynamic signal analyzer drives the shaker through an amplifier with an input voltage of sinusoidal signal so as to control the amplitude and frequency of the shaker. The dc power supply charges the MEMS device. The charge amplifier is used to convert charge change between movable and fixed combs of the device due to the excited vibration into output-voltage change, which is recorded by the dynamic signal analyzer.

The maximum voltage V_{max} of the variable capacitor of our device is given by

$$V_{\text{max}} = \frac{C_{\text{max}} + C_p}{C_{\text{min}} + C_p} V_{\text{start}} \quad (4)$$

where V_{start} is the input voltage by a dc power supply, which is used to charge the variable capacitor of the device, C_p is the parasitic capacitance due to substrates and anchors, and the capacitance changes from C_{max} to C_{min} due to ambient vibration-driven displacement.

Equation (4) can be easily expressed as

$$\frac{V_{\text{max}} - V_{\text{start}}}{V_{\text{start}}} = \frac{C_{\text{max}} - C_{\text{min}}}{C_{\text{min}} + C_p}. \quad (5)$$

Based on equation (5), we can obtain the capacitance change ΔC ($C_{\text{max}} - C_{\text{min}}$) because the voltage change ΔV ($V_{\text{max}} - V_{\text{start}}$) is recorded by the dynamic signal analyzer.

The energy being converted in one energy cycle can be written as

$$\begin{aligned} E &= \frac{1}{2} V_{\text{start}}^2 \frac{C_{\text{max}}}{C_{\text{min}}} (C_{\text{max}} - C_{\text{min}}) \\ &= \frac{1}{2} V_{\text{start}} V_{\text{max}} (C_{\text{max}} - C_{\text{min}}). \end{aligned} \quad (6)$$

As suggested in [4] and [11], a parallel capacitor, C_{par} , will be connected in parallel to the MEMS capacitor to limit the maximum voltage that is reached by the system.

The output power, averaged over time, for the load condition that maximized the transfer coefficient is

$$P = Ef. \quad (7)$$

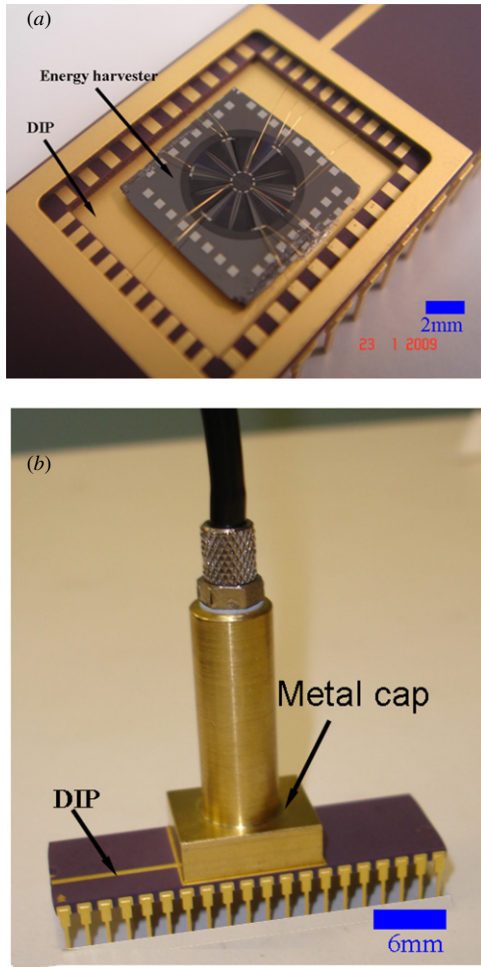


Figure 8. (a) The rotary comb energy harvester after wire bonding to DIP of 40 pins and (b) packaged prototype for vacuum testing.

Figures 8(a) and (b) show the prototype after wire bonding to a dual-in-line package (DIP) with 40 footprints and vacuum-packaged prototype, respectively. A dc operation mode circuit [14] is set up to measure the power. The schematic of the dc circuit is composed of an auxiliary battery supply V_{in} , a vibration-driven variable capacitor C_{MEMS} and an output storage capacitor C_{stor} connected with the loading resistance R_L , as shown in figure 9. The switches SW1, SW2 and SW3 are diodes [48]. When C_{MEMS} is charged to V_{in} , SW1 is opened and the capacitance is changed from C_{max} to C_{min} due to the excited vibration. In this process, the charge on the MEMS variable capacitor remains constant (SW1 and SW2 both open). Therefore, the terminal voltage on the MEMS capacitor is increased, converting the vibration energy into electrical energy stored in C_{MEMS} . The voltage change of the MEMS capacitor is monitored by the dynamic signal analyzer. When its terminal voltage achieves the maximum value of V_{max} , the MEMS capacitor reaches C_{min} , and vice versa. When the MEMS capacitor reaches C_{min} , SW2 is closed and C_{stor} is charged by C_{MEMS} by charge redistribution. SW2 is then opened and C_{MEMS} changes back to C_{max} , preparing for the next conversion cycle. During this period, the charge on C_{stor} is dissipated through the loading resistance R_L . In this mode, a dc current is generated due to the change from C_{min} to C_{max} ,

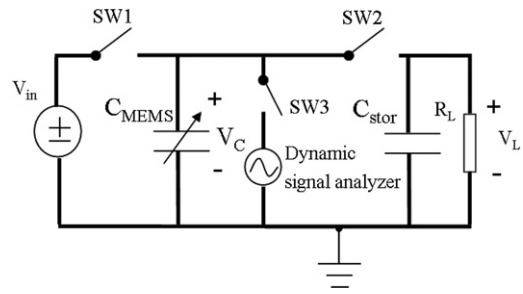


Figure 9. DC testing circuit schematic of an electrostatic energy converter.

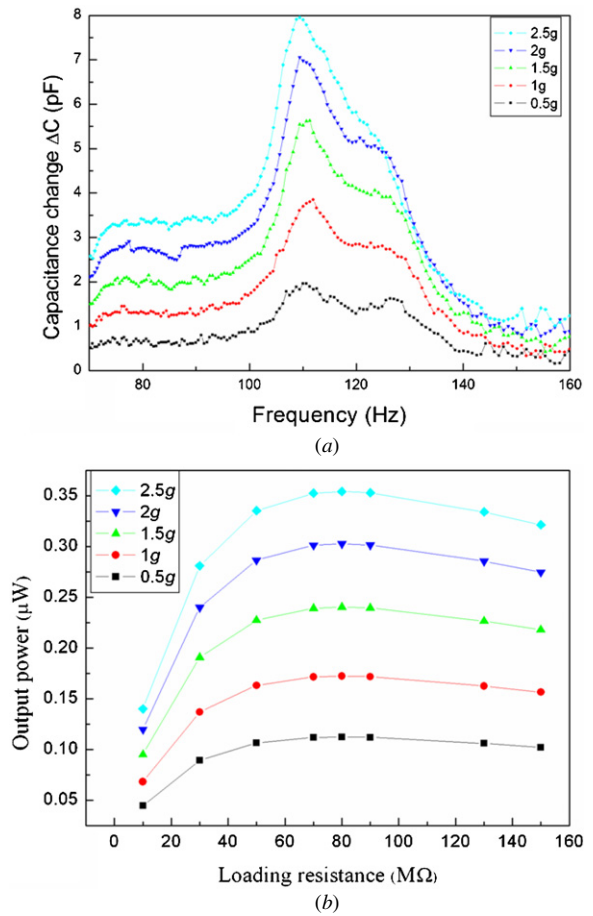


Figure 10. (a) The capacitance change versus resonant frequency under the acceleration of 0.5 g to 2.5 g in air; and (b) measured output power versus loading resistance under the acceleration of 0.5 g to 2.5 g in air.

which results in the output power to the loading resistance. The output voltage for various loading resistances is recorded by the dynamic signal analyzer.

In a testing setup, the prototype is fixed into the shaker and excited along the horizontal plane of the rotary comb, i.e. the in-plane vibration. Figure 10(a) shows the relationship between the capacitance change of one set of fixed combs and movable combs and excited frequency under various accelerations in air, i.e. from 0.5 g to 2.5 g. The measured total value of the parasitic capacitance C_p and the minimum capacitance C_{min} between one set of fixed combs and movable

combs is 5.2 pF. The bias voltage applied by dc power supply is 1 V. The observed maximum capacitance change, ΔC , occurs at 110 Hz. It means the resonant frequency of the rotary comb energy harvester is 110 Hz. The maximum ΔC is 2 and 8 pF for vibrations of 0.5 g and 2.5 g, respectively. Since there are 12 sets of rotary combs in one energy harvester, the maximum ΔC of the whole device in one vibration cycle is derived as 24 and 96 pF, respectively. For calculating the output energy and power, it is necessary to take into account the relationship among the parameters C_{\max} , C_{\min} , C_{par} , V_{start} and V_{\max} as well as the practical circuit constraints [4, 11, 27]. This is required in practice because circuits are only able to tolerate voltages below a certain limit, above which the switches in the circuit will break down. In the present demonstration, V_{start} is selected to be limited to 5 V and the V_{\max} to be below 20 V. Because it meets the requirement of this circuit constraint, the C_{par} in the dc operation mode circuit is not included in this testing. Based on equations (6) and (7), the electrical energy generated in one vibration cycle for vibrations of 0.5 g and 2.5 g is calculated as 1.2 nJ and 4.8 nJ, respectively, while the corresponding average output power is 0.132 μW and 0.528 μW , respectively.

The impedance of the MEMS variable capacitor without vibration is measured by the Agilent 4284A LCR meter. It shows that the parallel parasitic resistance is about 80 M Ω . The input vibration of the shaker is a 110 Hz sine wave under different accelerations. Figure 10(b) shows the output power under different loading resistances. A maximum output power for vibrations of 0.5 g, 1 g, 1.5 g, 2 g and 2.5 g is 0.11 μW , 0.17 μW , 0.24 μW , 0.3 μW and 0.35 μW , respectively, when the loading resistance matches the parasitic resistance of 80 M Ω . The measured output power is smaller than the calculated power due to the effect of electrical and mechanical damping in testing circuits. The electrical damping force [49] is given by

$$F_e(z) = \frac{Q^2}{2C_0} \frac{1}{(z + x_0)^2} \quad (8)$$

where Q is the initial charge on the capacitor, z is the overlap movement, x_0 is the initial gap overlap and C_0 is the capacitance per given length given by

$$C_0 = \frac{N_g \epsilon t}{g} \quad (9)$$

where N_g is the number of gaps in the rotary comb drive. It can be seen that the electrical damping force is not proportional to velocity, which is required for a harmonic oscillation. Thus, the motion will be inherently nonlinear. Moreover, in the case of Coulomb-damped resonators operated at a resonant frequency in the absence of parasitic damping and mechanical stoppers, the motion amplitude can continuously increase without limitation unless the damping force satisfies a stability criterion [50]:

$$F_e \geq \frac{\pi}{4} m \omega^2 Y_0. \quad (10)$$

High electrical damping is used to increase the bandwidth of the device. To achieve high conversion efficiency, the charge–discharge cycles and the operations of the switches must be timed precisely with the variation of the capacitance.

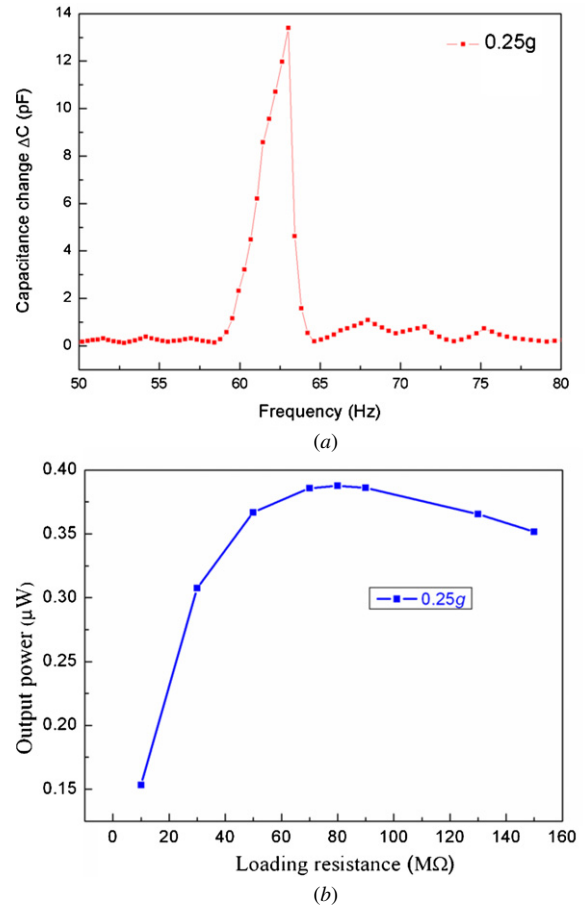


Figure 11. (a) The capacitance change versus resonant frequency at the pressure level of 3 Torr and the acceleration of 0.25 g; (b) measured output power versus loading resistance at the pressure level of 3 Torr and the acceleration of 0.25 g.

On the other hand, air damping is considered as having the key role in the dynamic response of actuation. In order to investigate the effect of air damping on the output performance of the device, the DIP package is sealed with a metal cap as shown in figure 8(b), and then the device chamber is pumped using PFEIFFER vacuum equipment (D-35614 Assiar model: TSH071) to achieve a desired vacuum level. Capacitance versus excited frequency only at the acceleration of 0.25 g is plotted in figure 11(a), and it is tested at the pressure level of 3 Torr. The maximum capacitance change of one set of combs and the total capacitance change are 13.4 pF and 160.8 pF at the resonant frequency of 63 Hz, respectively. Compared to the testing results shown in figure 10(a), larger capacitance change is obtained at lower vibration acceleration and narrower frequency bandwidth is observed due to smaller damping coefficient at the pressure level of 3 Torr. The calculated electrical energy collected in one vibration cycle and average output power for 0.25 g vibrations are 8 nJ and 0.504 μW , respectively. Based on the above-detailed dc circuit, the measured output power under different loading resistances is shown in figure 11(b), and the maximum power obtained under the resonant frequency for 0.25 g vibrations is 0.39 μW . The working conditions and output behavior of this MEMS energy harvesting device

Table 3. Comparison among MEMS electrostatic energy harvesting devices.

Author	Frequency (Hz)	Input acceleration (m s^{-2})	Volume (mm^3)	Power (μW)	Power density ($\mu\text{W cm}^{-3}$)
Menigier <i>et al</i> [11]	2520	–	75	8 ^a	106
Kuehne <i>et al</i> [13]	1000	1.96	–	4.28 ^a	–
Chiu <i>et al</i> [14]	1870	32.5	600	1.2	2
Hoffmann <i>et al</i> [26]	1460	130	–	0.6	–
Despesse <i>et al</i> [29]	50	8.8	1800	1052	584
Basset <i>et al</i> [30]	250	2.5	61.49	0.061	0.99
Arakawa <i>et al</i> [34]	10	3.9	400	6	15
Lo <i>et al</i> [37]	50	576.6	50 000	18	0.36
Naruse <i>et al</i> [39]	2	4	–	40	–
Mitcheson <i>et al</i> [54]	30	50	750	3.7 ^a	4.93
Mizuno <i>et al</i> [55]	743	13.9	600	7.4e-4	1.23e-3
Yang <i>et al</i> (measured at 1 atm in this research)	110	25	39.4	0.35	8.88
Yang <i>et al</i> (measured at 3 Torr in this research)	63	2.5	39.4	0.39	9.9

^aSimulated values.

together with other published electrostatic generators are listed in table 3 for comparison. It shows that the power density reported in this paper demonstrates comparable performance.

There is good agreement between simulated first resonant frequency (67.2 Hz) and measured frequency (63 Hz) at the pressure level of 3 Torr. But the first resonant frequency of the FEA result is smaller than the one tested in air, in which the energy loss due to squeeze-film damping dominates when it exists, as in the case of capacitive-based driven and sensed MEMS [51, 52]. In the rotary comb structures, as one side of the movable combs moves toward a set of fixed combs, it forces air out of the gap between comb fingers, causing a damping force, and compresses the air in the gap, causing a spring force, which results in an increased spring constant and correspondingly increased resonant frequency. Mohite *et al* [53] have observed the increased stiffness coefficient between a diaphragm and a perforated back plate due to the reduced air gap. In this paper, the experiment results show that the measured first resonant frequency in air is higher than the one in vacuum.

5. Conclusion and future work

An electrostatic energy harvester converting 2D in-plane vibration energy into electrical energy is demonstrated. A CMOS compatible process with two masks is developed to fabricate the harvester. In order to obtain a large capacitance change, i.e. larger rotation angles under the same excited acceleration for the energy harvester, the ladder spring is selected and simulated in this paper. The maximum capacitance change in air occurs at the first resonant frequency of 110 Hz. It is 2, 3.9, 5.6, 7 and 8 pF for vibrations of 0.5 g, 1 g, 1.5 g, 2 g, and 2.5 g, respectively. Maximum measured output power for vibrations of 0.5 g, 1 g, 1.5 g, 2 g and 2.5 g is 0.11 μW , 0.17 μW , 0.24 μW , 0.3 μW and 0.35 μW , respectively, when the loading resistance matches the parasitic resistance of 80 M Ω at the resonant frequency. The effect of air damping on output performance has been characterized. The measured results show that the resonant frequency at the pressure level of 3 Torr decreases from 110 Hz measured in

air to 63 Hz and the maximum electrical output power of 0.25 g acceleration arrives at 0.39 μW .

Acknowledgment

The authors thank the testing support from Institute of Microelectronics (IME), A*STAR. This research is partially funded by A*STAR HOME 2015 National Research Programme (SERC grant number: 0621150043) and by National University of Singapore under grant no R-263-000-475-112.

References

- [1] Beeby S P, Tudor M J and White N M 2006 Energy harvesting vibration sources for microsystems applications *Meas. Sci. Technol.* **17** R175–95
- [2] Arnold D P 2007 Review of microscale magnetic power generation *IEEE Trans. Magn.* **43** 3940–51
- [3] Hudak N S and Amatucci G G 2008 Small-scale energy harvesting through thermoelectric, vibration, and RF power conversion *J. Appl. Phys.* **103** 101301
- [4] Roundy S, Wright P K and Rabaey J 2003 A study of low level vibrations as a power source for wireless sensor nodes *Comput. Commun.* **26** 1131–44
- [5] Torah R, Glynn-Jones P, Tudor M, O'Donnell T, Roy S and Beeby S P 2008 Self-powered autonomous wireless sensor node using vibration energy harvesting *Meas. Sci. Technol.* **19** 125202
- [6] Torfs T, Leonov V and Vullers R J M 2007 Pulse oximeter fully powered by human body heat *Sensors Transducers* **80** 1230–8
- [7] Huesgen T, Woias P and Kockmann N 2008 Design and fabrication of MEMS thermoelectric generators with high temperature efficiency *Sensors Actuators A* **145–146** 423–9
- [8] Yang S M, Lee T and Jeng C A 2009 Development of a thermoelectric energy harvester with thermal isolation cavity by standard CMOS process *Sensors Actuators A* **153** 244–50
- [9] Wang Z, Fiorini P, Leonov V and Hoof C V 2009 Characterization and optimization of polycrystalline Si_{70%}Ge_{30%} for surface micromachined thermopiles in human body applications *J. Micromech. Microeng.* **19** 094011

- [10] Xie J, Lee C, Wang M F, Liu Y and Feng H H 2009 Characterization of heavily doped polysilicon films for CMOS-MEMS thermoelectric power generators *J. Micromech. Microeng.* **19** 125029
- [11] Menigner S, Mur-Miranda J O, Amirtharajah R, Chandrakasan A P and Lang J H 2001 Vibration-to-electric energy conversion *IEEE Trans. Very Large Scale Integr. (VLSI) Syst.* **9** 64–76
- [12] Mitcheson P D, Miao P, Stark B H, Yeatman E M, Holmes A S and Green T C 2004 MEMS electrostatic micropower generator for low frequency operation *Sensors Actuators A* **115** 523–9
- [13] Kuehne I, Frey A, Marinkovic D, Eckstein G and Seidel H 2008 Power MEMS-A capacitive vibration-to-electrical energy converter with built-in voltage *Sensors Actuators A* **142** 263–9
- [14] Chiu Y and Tseng V F G 2008 A capacitive vibration-to-electricity energy converter with integrated mechanical switches *J. Micromech. Microeng.* **18** 104004
- [15] Bartsch U, Gaspar J and Paul O 2010 Low-frequency two-dimensional resonators for vibrational micro energy harvesting *J. Micromech. Microeng.* **20** 035016
- [16] Glynne-Jones P, Tudor M J, Beeby S P and White N M 2004 An electromagnetic, vibration-powered generator for intelligent sensor systems *Sensors Actuators A* **110** 344–9
- [17] Beeby S P, Torah R N, Tudor M J, Glynne-Jones P, O'Donnell T, Saha C R and Roy S 2007 A micro electromagnetic generator for vibration energy harvesting *J. Micromech. Microeng.* **17** 1257–65
- [18] Sari I, Balkan T and Kulah H 2008 A electromagnetic micro power generator for wideband environmental vibrations *Sensors Actuators A* **145** 405–13
- [19] Yang B, Lee C, Xiang W F, Xie J, He H, Kotlanka R K, Low S P and Feng H H 2009 Electromagnetic energy harvesting from vibrations of multiple frequencies *J. Micromech. Microeng.* **19** 035001
- [20] Sari I, Balkan T and Kulah H 2009 An electromagnetic micro energy harvester based on an array of parylene cantilevers *J. Micromech. Microeng.* **19** 105023
- [21] Lu F, Lee H P and Lim S P 2004 Modeling and analysis of micro piezoelectric power generators for micro-electromechanical-systems applications *Smart Mater. Struct.* **13** 57–63
- [22] Jeon Y, Sood R, Jeong J H and Kim S G 2005 MEMS power generator with transverse mode thin film PZT *Sensors Actuators A* **122** 16–22
- [23] Shen D N, Park J H, Ajitsaria J, Choe S Y, H C W III and Kim D J 2008 The design, fabrication and evaluation of a MEMS PZT cantilever with integrated Si proof mass for vibration energy harvesting *J. Micromech. Microeng.* **18** 055017
- [24] Renaud M, Karakaya K, Sterken T, Fiorini P, Van Hoof C and Puers R 2008 Fabrication, modelling and characterization of MEMS piezoelectric vibration harvesters *Sensors Actuators A* **145–146** 380–6
- [25] Elfrink R, Kamel T M, Goedbloed M, Matova S, Hohlfeld D, Van An del Y and Van Schaijk R 2009 Vibration energy harvesting with aluminum nitride-based piezoelectric devices *J. Micromech. Microeng.* **19** 094005
- [26] Hoffmann D, Folkmer B and Manoli Y 2009 Fabrication, characterization and modelling of electrostatic micro-generators *J. Micromech. Microeng.* **19** 094001
- [27] Lee C, Lim Y M, Yang B, Kotlanka R K, Heng C H, He H, Tang M, Xie J and Feng H H 2009 Theoretical comparison of the energy harvesting capability among various electrostatic mechanisms from structure aspect *Sensors Actuators A* **156** 208–16
- [28] Chiu Y, Kuo C T and Chu Y S 2007 MEMS design and fabrication of an electrostatic vibration-to-electricity energy converter *Microsyst. Technol.* **13** 1663–9
- [29] Despesse G, Jager T, Chaillout J J, Léger J M, Vassilev A, Basrou S and Charlot B 2005 Fabrication and characterization of high damping electrostatic micro devices for vibration energy scavenging *Proc. DTIP'05* pp 386–90
- [30] Basset P, Galayko D, Mahmood Paracha A, Marty F, Dudka A and Bourouina T 2009 A batch-fabricated and electret-free silicon electrostatic vibration energy harvester *J. Micromech. Microeng.* **19** 115025
- [31] Mahmood Paracha A, Basset P, Galayko D, Marty F and Bourouina T 2009 A silicon MEMS DC/DC converter for autonomous vibration-to-electrical-energy scavenger *IEEE Electron. Device Lett.* **30** 481–3
- [32] Boland J, Chao C-H, Suzuki Y and Tai Y-C 2003 Micro electret power generator *16th IEEE Int. Conf. MEMS (Kyoto)* pp 538–41
- [33] Sterken T, Fiorini P, Baert K, Puers R and Borghs G 2003 An electret-based electrostatic μ -generator *Proc. Transducers'03 (8–12 June)* pp 1291–4
- [34] Arakawa Y, Suzuki Y and Kasagi N 2004 Micro seismic power generator using electret polymer film *Power MEMS Conf (Kyoto, Japan)* pp 187–90
- [35] Tsutsumino T, Suzuki Y, Kasagi N and Sakane Y 2006 Seismic power generator using high-performance polymer electret *19th IEEE Int. Conf. MEMS '06 (Istanbul)* pp 98–101
- [36] Ma W, Zhu R, Rufer L, Zohar Y and Wong M 2007 An integrated floating-electrode electric microgenerator *J. Microelectromech. Syst.* **16** 29–37
- [37] Lo H-W and Tai Y-C 2008 Parylene-based electret power generators *J. Micromech. Microeng.* **18** 104006
- [38] Sakane Y, Suzuki Y and Kasagi N 2008 The development of a high-performance perfluorinated polymer electret and its application to micro power generation *J. Micromech. Microeng.* **18** 104011
- [39] Naruse Y, Matsubara N, Mabuchi K, Izumi M and Suzuki S 2009 Electrostatic micro power generation from low-frequency vibration such as human motion *J. Micromech. Microeng.* **19** 094002
- [40] Yeatman E M 2008 Energy harvesting from motion using rotating and gyroscopic proof masses *Proc. Inst. Mech. Eng. C* **222** 27–36
- [41] Bartsch U, Gaspar J and Paul O 2009 A 2D electret-based resonant micro energy harvester *Proc. IEEE MEMS Conf. (Sorrento, Italy)* pp 1043–6
- [42] Jill J D, Zhang Y, Grade J D, Lee H, Hrinya S and Jerman H 2001 Widely tunable external cavity diode laser based on a MEMS electrostatic rotary actuator *IEEE Proc. Opt. Fiber Commun. Conf. Exhibit (Optical Society of America, Washington, DC, 2001)* vol 2 TuJ2-1–TuJ2-3
- [43] Yeh J A, Chen C N and Lui Y S 2005 Large rotation actuated by in-plane rotary comb-drive with serpentine spring suspension *J. Micromech. Microeng.* **15** 201–6
- [44] Lim T S, Ji C H, Oh C H, Kwon H, Yee Y and Bu J U 2004 Electrostatic MEMS variable optical attenuator with rotating folded micromirror *IEEE J. Sel. Top. Quantum Electron.* **10** 558–62
- [45] Yeh J A, Jiang S S and Lee C 2006 MOEMS variable optical attenuators using rotary comb drive actuators *IEEE Photonics Technol. Lett.* **18** 1170–2
- [46] Tu C C, Fanchiang K and Liu C H 2006 Rotary electrostatic micromirror switches using wafer-scale processing and assembly *Microsyst. Technol.* **12** 1099–108

- [47] Hou Max T K, Huang J Y, Jiang S S and Yeh J A 2008 In-plane rotary comb-drive actuator for a variable optical attenuator *J. Micro/Nanolith. MEMS MOEMS* **7** 043015
- [48] Roundy S, Wright P K and Rabaey J M 2003 *Energy Scavenging for Wireless Sensor Networks with Special Focus on Vibrations* (Dordrecht: Kluwer)
- [49] Mitcheson P D, Reilly E K, Toh T, Wright and Yeatman E M 2007 Performance limits of the three MEMS inertial energy generator transduction types *J. Micromech. Microeng.* **17** S211–6
- [50] Den Hartog J P 1985 *Mechanical Vibrations* (Mineola, NY: Dover)
- [51] Hosaka H, Itao K and Kuroda S 1995 Damping characteristics of beam-shaped micro-oscillators *Sensors Actuators A* **49** 87–95
- [52] Corman T, Enoksson P and Stemme G 1997 Gas damping of electrostatically excited resonators *Sensors Actuators A* **61** 249–55
- [53] Mohite S S, Kesari H, Sonti V R and Pratap 2005 Analytical solutions for the stiffness and damping coefficients of squeeze films in MEMS devices with perforated back plates *J. Micromech. Microeng.* **15** 2083–92
- [54] Mitcheson P, Stark B, Miao P, Yeatman E, Holmes A and Green T 2003 Analysis and optimization of MEMS on-chip power supply for self powering of slow moving sensors *Proc. Euroensors XVII (Guimaraes, Portugal)* pp 30–1
- [55] Mizuno M and Chetwynd D G 2003 Investigation of a resonance microgenerator *J. Micromech. Microeng.* **13** 209–16